

Physical Model for the Current–Voltage Hysteresis and Impedance of Halide Perovskite Memristors

Mariana Berruet, José Carlos Pérez-Martínez, Beatriz Romero, Cedric Gonzales, Abdullah Al-Mayouf, Antonio Guerrero, and Juan Bisquert*



Cite This: <https://doi.org/10.1021/acsenerylett.2c00121>



Read Online

ACCESS |



Metrics & More

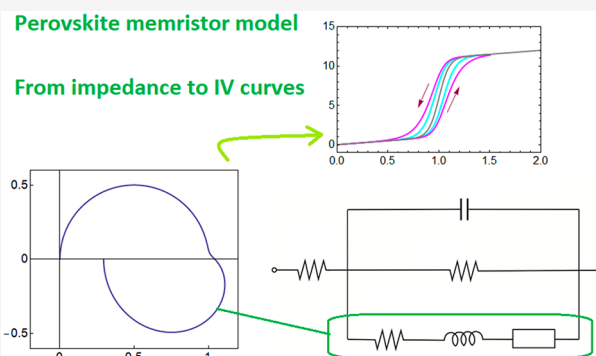


Article Recommendations



Supporting Information

ABSTRACT: An investigation of the kinetic behavior of MAPbI₃ memristors shows that the onset voltage to a high conducting state depends strongly on the voltage sweep rate, and the impedance spectra generate complex capacitive and inductive patterns. We develop a dynamic model to describe these features and obtain physical insight into the coupling of ionic and electronic properties that produce the resistive switching behavior. The model separates the memristive response into distinct diffusion and transition-state-formation steps that describe well the experimental current–voltage curves at different scan rates and impedance spectra. The ac impedance analysis shows that the halide perovskite memristor response contains the composition of two inductive processes that provide a huge negative capacitance associated with inverted hysteresis. The results provide a new approach to understand some typical characteristics of halide perovskite devices, such as the inductive behavior and hysteresis effects, according to the time scales of internal processes.



In less than a decade, metal halide perovskite (MHP) materials have established a new photovoltaic (PV) technology that demonstrated very large solar energy conversion efficiencies with low-cost, solution-processed materials.^{1–4} The MHP can be described as ABX₃ where A is a monovalent cation such as methylammonium (MA), formamidinium (FA), or cesium (Cs); B is a divalent cation such as lead (Pb) or tin (Sn); and X is a halide anion, including chloride (Cl), bromide (Br), and iodide (I). MHP semiconductors show mixed ionic–electronic conduction in which a significant ionic conductivity due to vacancy displacements exists in addition to the electronic photoconductivity.^{5–8} These properties are difficult to measure because of the intersection of very different time scales of ionic and electronic effects that interact with each other. They cause intrinsic memory effects (hysteresis) in current–voltage (*I–V*)^{9–14} that lead to substantial differences in the forward and reverse scan currents and permanent resistive changes. These features are highly significant for important new applications in which MHPs are used for nonoptoelectronic applications related to memory storage and brain-like computation. Herein, on the basis of previous understanding of the MHP solar cells,^{9,15} we develop a physical model to describe the results of MHP

memristors in both voltage cycling and impedance spectroscopy.

A memristor is a two-terminal device whose resistance depends on the history of current and voltage applied to the device. Memristors allow the storage of information by metastable modification of device conductivity.^{16–20} Typically, a memristor makes a transition from a high to a low resistance state (HRS–LRS) when a certain threshold forward voltage is passed, which can be restored to the initial state by a reverse voltage sweep.^{18,21,22} There has been rapid recent progress in perovskite memristor endurance performance²³ that facilitates application to resistive RAM.²⁴ Synaptic plasticity, the ability of the connection between neurons to strengthen or weaken by external stimulation, is a central property in the operation of neuronal circuits. The development of spiking neural networks requires a precise control of the functionality of synapses,⁵⁹

Received: January 17, 2022

Accepted: February 23, 2022

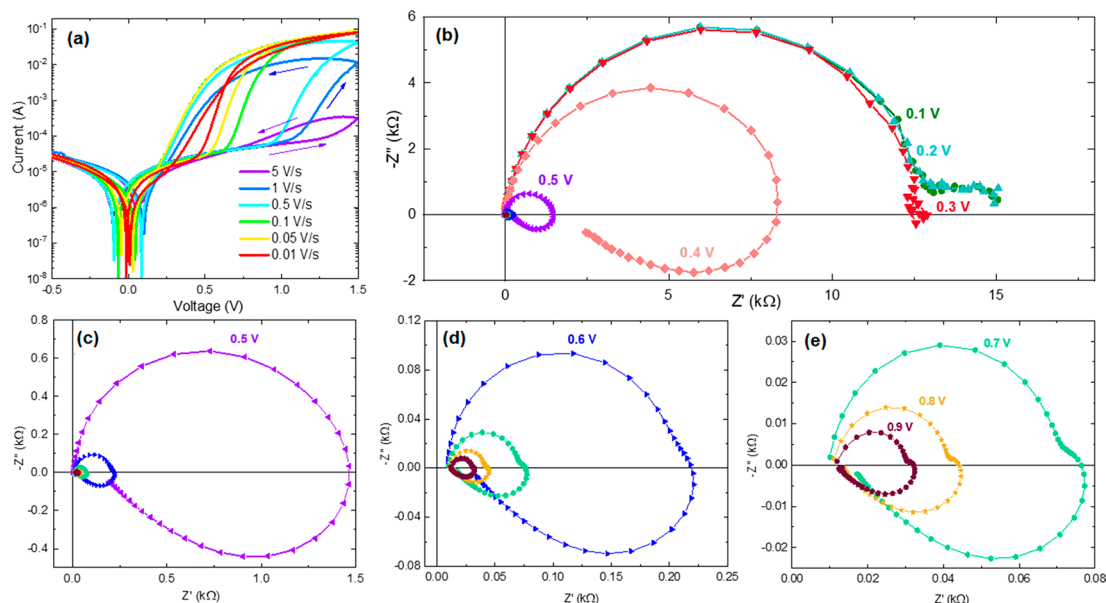


Figure 1. (a) Current–voltage characteristic for an FTO/PEDOT:PSS/MAPI/Au memristor device at 6 different scan rates starting from 5 V/s. Arrows indicate sweep direction. (b–e) Complex plane plot representation of the impedance spectra at different applied dc voltage. Panels c, d, and e correspond to a magnification of the scales.

60 neurons, and their assemblies by the properties of plasticity,
 61 adaptation, spiking, and the synchronization of the temporal
 62 dynamics and shapes of repetitive spikes and their integra-
 63 tion.^{25,26} Currently, there is great interest in developing
 64 bio-realistic elements that contain no internal circuitry.²⁷ MHP
 65 memristors that undergo a relatively slow transition to HRS
 66 take a leading role in the search for emulation of brain
 67 functions with assemblies of artificial synapse devices^{28–30} in
 68 neuromorphic computation.^{27,31,32} Furthermore, MHPs pro-
 69 vide photoactive synapses suitable to artificial vision devices in
 70 which the memory effects can be adapted for preprocessing of
 71 image data before transfer to the computing unit eliciting a
 72 motor response.^{33–35}

73 In order to design material properties for these applications
 74 it is necessary to establish the precise properties of time
 75 dynamics of memristors and their response and changes under
 76 repetitive stimuli at varying frequency. Impedance spectroscopy
 77 (IS) consists of the electrical measurement of current-to-
 78 voltage of the device at a steady-state potential V by small
 79 perturbation at changing angular frequency ω . It is a central
 80 technique for the characterization of PV cells and electro-
 81 chemical devices.^{15,36} We have recently shown that a precise
 82 connection can be established between the frequency and time
 83 domain in the analysis of hysteresis and time transients of PV
 84 devices.^{9,37} However, memristors with extreme hysteresis
 85 effects have so far not been described with IS models that
 86 can predict hysteresis and time transient behavior to determine
 87 the physical basis for parameters such as the switching speed
 88 and the retention time.

89 Herein, we take a first step in this direction. We analyze the
 90 properties of glass/FTO/PEDOT:PSS/MAPbI₃/Au perov-
 91 skite-based memristor devices.^{38,39} The details of device
 92 preparation are provided in the Supporting Information.
 93 Figure 1 shows the characterization in I – V sweeps of a typical
 94 threshold resistive switching device where the switching event
 95 is confined to one quadrant only.⁴⁰ We note that the effective
 96 onset of the transition occurs at higher voltage when the
 97 potential sweep is at higher scan rate. The device exhibits ON

state retention times of $>10^4$ s at a read voltage of 0.5 V⁹⁸
 (Figure S11b), rendering them suitable for volatile memory⁹⁹
 applications (Figure S11c). At the beginning, the ON state¹⁰⁰
 current exponentially decreases but then stabilizes at 38% of¹⁰¹
 the initial value, maintaining an ON/OFF ratio of ~ 1 order of¹⁰²
 magnitude. Voltage-dependent IS response was performed via¹⁰³
 a sequence of chronoamperometry (CA) measurement for 10¹⁰⁴
 s, subsequently followed by IS with a frequency range of 0.1¹⁰⁵
 MHz to 0.1 Hz. We note that active areas are very large (0.25¹⁰⁶
 cm²) for memory applications, but this area helps to maximize¹⁰⁷
 the impedance response reducing the noise in the low-¹⁰⁸
 frequency region. When devices are scaled to areas of $\sim 10^5$ ¹⁰⁹
 μm^2 , the trends of the I – V curves hold, indicating that the¹¹⁰
 main switching mechanism is maintained but the IS response is¹¹¹
 noisy (Figure S12). In any case, the model is still useful to¹¹²
 extract different properties of other large-area applications such¹¹³
 as solar cells or LEDs.¹¹⁴

Figure 1b–e shows the impedance spectra at different¹¹⁵
 applied voltage from 0.1 to 0.9 V. At low voltage the device¹¹⁶
 responds with a double RC arc as is found in solar cell¹¹⁷
 perovskite devices.¹⁵ At 0.3 V and higher voltages a large¹¹⁸
 inductor component at low frequency is formed that is also¹¹⁹
 typical of perovskite solar cells at high voltage, which causes a¹²⁰
 negative capacitance effect.^{9,41–43} This feature has been¹²¹
 reported before in perovskite memristors.³⁹ For 0.5 V and¹²²
 higher the crossing of the real axis of the impedance complex¹²³
 plane shows a strong rightward distortion. This last feature has¹²⁴
 not been described before, but it is highly reproducible as¹²⁵
 shown in the Supporting Information with the results of¹²⁶
 another sample (Figure S13).¹²⁷

We aim to establish the simplest models that can explain the¹²⁸
 observed properties of IS and current voltage curves at¹²⁹
 different scan rates, accounting qualitatively for the strong¹³⁰
 memory effect and resistive switching phenomena. Our model¹³¹
 is adapted to those perovskite memristors that show a gradual¹³²
 transition in current–voltage scans so that the change of¹³³
 conductance can be regulated by the voltage amplitude and¹³⁴
 operation time.³² These properties allow us to faithfully¹³⁵

136 replicate the nature of plasticity in synapses.²⁸ We adopt a
 137 method related to the dynamic systems of neurons,^{44,45} of the
 138 class of fast–slow dynamic models,⁴⁶ that describes rather
 139 complex phenomena with a relatively simple number of
 140 differential equations, like the two-dimensional FitzHugh–
 141 Nagumo neuron model.⁴⁷ Another famous model of this type
 142 is the Hodgkin–Huxley (HH) model.⁴⁸ It is four dimensional
 143 with a fast variable (the voltage across the cell membrane) and
 144 several slow variables that describe the conduction state of a
 145 particular voltage-gated ion channel, which can be open or
 146 closed according to the value of the membrane voltage. In the
 147 HH model the channel state is described by a continuous
 148 function that varies from 0 to 1 and obeys a first-order kinetic
 149 equation for the evolution to the voltage-driven equilibrium
 150 state.^{44,49} We will utilize this type of state variable in our model
 151 as well. In the following paragraphs, we develop the main
 152 model and several simplified cases. The expressions and
 153 properties are listed in Tables 1, 2, and 3.

Table 1. Main Equations of This Work

equation
$I_{\text{tot}} = C_m \frac{du}{dt} + \frac{u}{R_b} + i_c \quad (1)$
$\tau_d \frac{di_c}{dt} = i_{c0} f - i_c \quad (2)$
$\frac{df}{dt} = k_0(1-f) - k_1 f \quad (3)$
$f(u) = \frac{1}{1 + e^{-(u-V_T)/V_m}} \quad (4)$
$\tau_k \frac{df}{dt} = e^{\alpha(u-V_T)/V_m}(1-f) - e^{(\alpha-1)(u-V_T)/V_m} f \quad (5)$
$\tau_d \frac{di_c}{dt} = i_{c0} \frac{1}{1 + e^{-(u-V_T)/V_m}} - i_c \quad (6)$
$I_{\text{tot}} = C_m \frac{du}{dt} + \frac{u}{R_b} + i_{c0} f \quad (7)$
$I_{\text{tot}} = C_m \frac{du}{dt} + qN \frac{df}{dt} + \frac{u}{R_b} + i_{c0} f \quad (8)$
$I_{\text{tot}} = C_m \frac{du}{dt} + qN \frac{df}{dt} + \frac{u}{R_b} + i_c \quad (9)$

154 The models we propose describe the evolution of the
 155 external variables of the MHP memristor, namely, the total
 156 current I_{tot} and the voltage across the internal contacts, u ,
 157 under a certain stimulus out of equilibrium, influenced by two
 158 internal variables, i_c and f , that obey the set of dynamic
 159 equations (eqs 1–3) indicated in Table 1. These equations
 160 define model 1 in Table 3. In this model, we adopt a number of
 161 premises to describe the experimental observations. The
 162 conduction current I_{tot} has three components, as indicated in
 163 eq 1: a capacitive charging of the interfaces with capacitance
 164 C_m , a small ohmic current of constant resistance R_b , and a slow-
 165 responding current i_c with a large saturation value i_{c0} . Very
 166 different mechanisms for the formation of the LRS have been
 167 suggested in the literature, according to different materials and
 168 configurations: (1) formation of a filamentary conductive
 169 pathway,¹⁸ (2) decrease of a surface barrier by ion-assisted
 170 electrochemical interactions between the perovskite and
 171 contacts,^{38,50} and (3) decrease of the surface barrier by
 172 formation of ion-assisted self-doped regions in the vicinity of

Table 2. Impedance Spectroscopy Models of This Work

equation	figure
$Z(s) = \left[C_m s + R_b^{-1} + \frac{1}{Z_c} \right]^{-1} \quad (10)$	3e
$Z_c(s) = (1 + s\tau_d)(R_a + L_a^k s) \quad (11)$	
$R_a^{-1} = \frac{di_c}{du} = \frac{i_{c0}}{V_m} f(1-f) \quad (12)$	
$L_a^k = f\tau_k R_a \quad (13)$	
$L_a^d = \tau_d R_a \quad (14)$	
$Z_c(\omega) = R_a + i\omega L_a^k + i\omega L_a^d + R_c(\omega) \quad (15)$	
$R_c(\omega) = -\frac{L_a^k L_a^d}{R_a} \omega^2 \quad (16)$	
$Z(s) = \left[C_m s + R_b^{-1} + \frac{1}{R_a + L_a^k s} \right]^{-1} \quad (17)$	3a
$Z(s) = \left[C_m s + R_b^{-1} + \frac{1}{R_a + L_a^k s} + \frac{1}{R_2 + \frac{1}{C_2 s}} \right]^{-1} \quad (18)$	3c
$R_2 = \frac{L_a^k i_{c0}}{Q_m} \quad (19)$	
$C_2 = \frac{Q_m}{R_a i_{c0}} \quad (20)$	
$Z(s) = \left[C_m s + R_b^{-1} + \frac{1}{R_2 + \frac{1}{C_2 s}} + \frac{1}{Z_c} \right]^{-1} \quad (21)$	S18

Table 3. Different Models of This Work

denomination	variables	time constants	dynamic equations	impedance function
(1) full transition model	u, i_c, f	$\tau_m, \tau_d, f\tau_k$	1, 2, 5	9
(2) diffusion-limited	u, i_c	τ_m, τ_d	1, 6	16, $L_a = L_a^d$
(3) formation-limited	u, f	$\tau_m, f\tau_k$	7, 5	16, $L_a = L_a^k$
(4) formation and capacitance	u, f	$\tau_m, f\tau_k, \tau_2$	8, 5	17
(5) inductors and capacitance	u, i_c, f	$\tau_m, \tau_d, f\tau_k, \tau_2$	9, 2, 5	21

173 interfaces.²⁷ These physical transformations are often asso-
 174 ciated with general ion migration effects. In this work, we do
 175 not attempt to clarify the mechanism of the investigated
 176 memristor, which requires an in-depth investigation of
 177 materials and contact properties that will be presented
 178 elsewhere. However, in order to describe the complex dynamic
 179 properties that have been observed by voltammetry and IS, we
 180 will separate clearly two features in the transition to the LRS:

- (a) The onset of conduction in quasi-equilibrium depends
 181 on a threshold voltage V_T connected to the material
 182 properties (bulk and interface). The activation of the
 183 high current component i_c occurs by the change of an
 184 occupation function $0 \leq f \leq 1$ that is controlled by the
 185 voltage. Similar to the ion channel behavior in neurons,
 186 the variable f indicates the state of the mechanism that
 187 establishes the high-conductivity state up to the limiting
 188 current i_{c0} . Equation 3 is a reaction equation with rate
 189 constants k_0 and k_1 that describes the voltage-controlled
 190 activation of the high-conduction configuration. 191

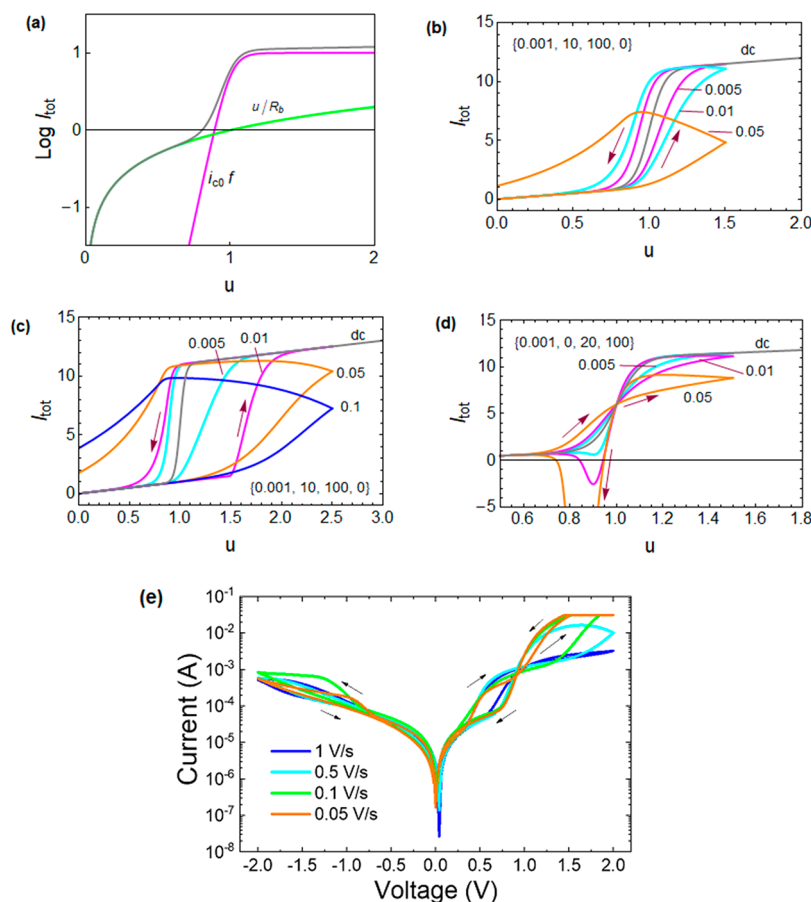


Figure 2. (a) Logarithmic current–voltage curve for model 1 memristor. The gray line is the total equilibrium dc current. (b) Current at forward and backward scan of model 1 at different rates as indicated, $\alpha = 0$, $V_m = 0.05$, and (c) $\alpha = 0.1$, $V_m = 0.025$. Parameters $R_b = 1$; $i_{c0} = 10$, $V_T = 1$, $[\tau_m, \tau_d, \tau_k, Q_m]$. (d) Current at forward and backward scan for model 4 at different rates as indicated, $\alpha = 0$, $V_m = 0.05$. (e) Current–voltage characteristic for an FTO/PEDOT:PSS/MAPI/Spiro-MeOTAD/Au device at 4 different scan rates.

192 (b) The observations indicate that the increase of f is also
 193 determined by the rate of ion transport. We introduce in
 194 eq 2 a delay of i_c with the characteristic time τ_d (eq 2).
 195 Typically, this temporal parameter represents a diffusion
 196 or migration time of ions, necessary to establish the
 197 configuration of high f that produces the large electronic
 198 current i_{c0} .

199 This model is an extension of the two-dimensional models
 200 that have been recently proposed to describe inductive
 201 behavior and inverted hysteresis in MHP and in neu-
 202 rons,^{9,15,45,51} and it is also an extension of the standard set
 203 of equations for a voltage-controlled memristor.^{19,52} Model 1
 204 of eqs 1–3 is three-dimensional and displays additional kinetic
 205 complexity that is necessary to account for the observed
 206 experimental behaviors of the memristor. We remark that eq 2
 207 is a rather simplified transport equation, and one may use drift-
 208 diffusion approaches in a more sophisticated treatment. In
 209 addition, the form of eq 3 is not unique but may depend
 210 strongly on the kinetics mechanisms and material properties,
 211 e.g., with higher-order reaction kinetics. Here we adopt eqs 2
 212 and 3 as the simplest reasonable assumption that illustrates the
 213 coupling of different steps in the overall model.

214 Let us analyze in more detail the properties of the dynamic
 215 model. It is important to find, first of all, the steady-state
 216 characteristics represented by current–voltage curves. By
 217 suppressing the time derivatives in eqs 1–3, we obtain the
 218 following conditions for a stationary state:

$$I_{\text{tot}} = \frac{u}{R_b} + i_c \quad (22) \quad 219$$

$$i_c = i_{c0}f \quad (23) \quad 220$$

$$k_0(1 - f) = k_1f \quad (24) \quad 221$$

The last equation can be stated 222

$$f(u) = \frac{1}{1 + \frac{k_1}{k_0}} \quad (25) \quad 223$$

By the detailed balance principle, this last equation 224
 corresponds to the equilibrium occupancy given by the 225
 Fermi–Dirac or Nernst equilibrium distribution function, eq 226
 4, where V_T is the redox potential of the activation state so that 227
 in the equilibrium line $f(V_T) = 0.5$. V_m in eq 4 is a constant 228
 with dimension of voltage, with a diode ideality factor m with 229
 respect to the thermal voltage $k_B T/q$, where T is the absolute 230
 temperature, k_B the Boltzmann constant, and q the elementary 231
 charge, so that $V_m = mk_B T/q$. Therefore, we obtain 232

$$\frac{k_0}{k_1} = e^{(u - V_T)/V_m} \quad (26) \quad 233$$

We introduce the kinetic time of the formation process τ_k . 234
 Then the reaction kinetic constants are expressed by a partition 235
 that satisfies eq 26:⁵³ 236

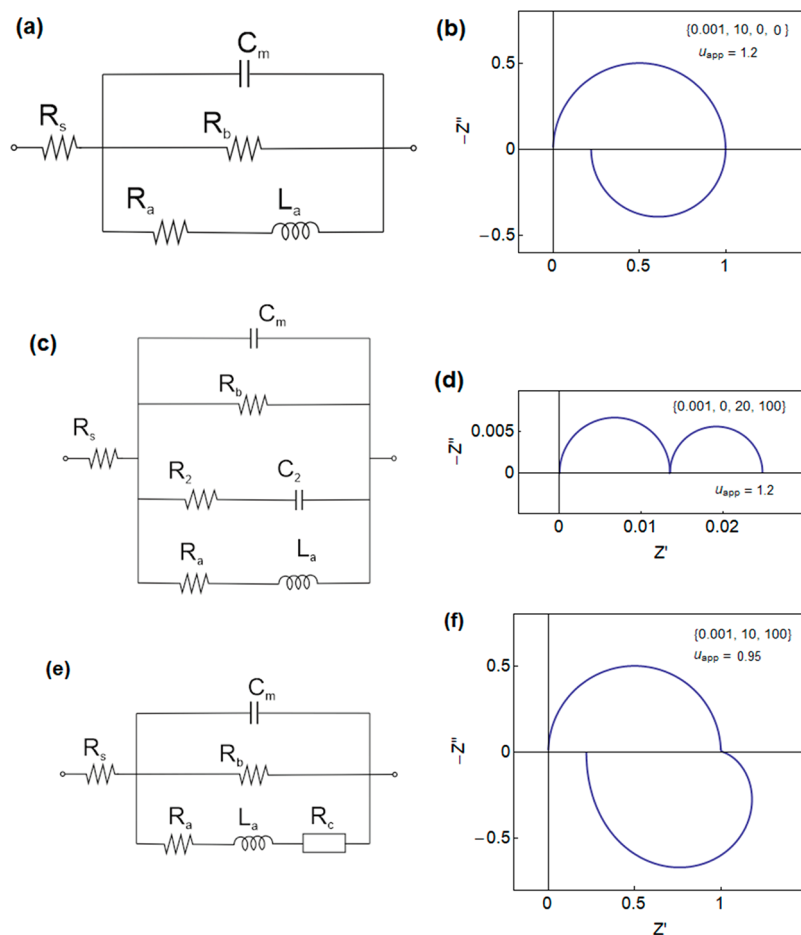


Figure 3. (a) Equivalent circuit model for diffusion-limited model 2 and formation-limited model 3. (b) Impedance spectrum of model 2 for parameters $R_b = 1$; $i_{c0} = 10$; $V_T = 1$; $\alpha = 0$; $V_m = 0.05$; $[\tau_m, \tau_d, \tau_k, Q_m]$. (c) Equivalent circuit model for surface capacitive model 4. (d) Impedance spectrum of model 4. (e) Equivalent circuit model for model 1. (f) Impedance spectrum of model 1.

$$k_0 = \tau_k^{-1} e^{\alpha(u-V_T)/V_m} \quad (27)$$

$$k_1 = \tau_k^{-1} e^{(\alpha-1)(u-V_T)/V_m} \quad (28)$$

The constant and $0 \leq \alpha \leq 1$ is a Tafel coefficient. We can write the dynamic eq 3 in the final form (eq 5). In the simulations the unit of time is s, voltage is V, current is A, and resistance is Ω . The steady-state current–voltage equation is

$$I_{app} = \frac{u_{app}}{R_b} + \frac{1}{1 + e^{-(u_{app}-V_T)/V_m}} i_{c0} \quad (29)$$

This is shown in Figure 2a. As stated before, the dc current is formed by two components: an ohmic baseline (green) and a large current that is onset at voltage V_T (magenta). This is the typical form of MHP memristors²⁷ as shown in Figure 1a.

Memristor dynamics are characterized by a rich variety of transient phenomena that our model is intended to describe. These will be determined by the three time parameters of model 1: $\tau_m = R_b C_m$, τ_d , and τ_k , which we assume to be constants. To analyze these questions, we present the results of CV, in which the current is measured under voltage sweep at scan rate v_r according to the expression

$$V(t) = V_0 + v_r t \quad (30)$$

This method reveals the famous hysteresis effects in current–voltage curves of solar cells.^{9,54–57} When we apply eq 30, the model eqs 1, 2, and 5 become

$$I_{tot} = \frac{u}{R_b} + i_c + C_m v_r \quad (31)$$

$$\tau_d v_r \frac{di_c}{du} = i_{c0} f - i_c \quad (32)$$

$$\tau_k v_r \frac{df}{du} = e^{\alpha(u-V_T)/V_m} (1-f) - e^{(\alpha-1)(u-V_T)/V_m} f \quad (33)$$

The two differential equations (32 and 33) can be solved with the chosen boundary conditions. In this case we take $f(u=0) = 0$ and $i_c(u=0) = 0$. The voltage-dependent $i_c(u)$ is inserted into eq 29. A set of simulation results of model 1 are presented in Figures 2b,c and SI4. The transition to high conduction happens at higher voltage for fast scan rates, as observed experimentally in Figure 1a. Figure 2c shows a wider separation between forward and backward scans due to a modification of α coefficient. Figure SI4g shows the distinctive conductivity levels that provide the synaptic property of the perovskite memristors by gradual analog switching.³² The model is valid for both volatile and nonvolatile memories as noted in Figure SI4.

To better understand the dynamic properties, we develop the method of IS. We apply a small perturbation procedure to

277 the dynamic equations and Laplace-transform the time
278 derivative to $s = i\omega$. The small amplitudes of the variables
279 are denoted \hat{x} . The resulting equations have the form

$$280 \quad \hat{I}_{\text{tot}} = \frac{\hat{u}}{R_b} + \hat{i}_c + C_m s \hat{u} \quad (34)$$

$$281 \quad \tau_d s \hat{i}_c = i_{c0} \hat{f} - \hat{i}_c \quad (35)$$

$$282 \quad \tau_k s \hat{f} = -\frac{\hat{f}}{f} - \frac{f(1-f)}{V_m} \hat{u} \quad (36)$$

283 We calculate the impedance $Z(s) = \hat{u}(s)/\hat{I}_{\text{tot}}(s)$ and we
284 obtain eqs 10 and 11 where R_a in eq 12 is a resistance and L_a^k
285 and L_a^d are inductors (eqs 13 and 14). These elements have
286 been explained in two-dimensional models in previous
287 publications^{15,51} in relation with negative capacitance and
288 hysteresis in MHP. However, model 1 is three-dimensional and
289 contains two inductive processes that are combined in eq 11.
290 This impedance introduces the two inductor elements in the
291 expression of eq 15 and furthermore introduces a negative and
292 frequency-dependent resistance $R_c(\omega)$, eq 16, not previously
293 reported in the literature, to our knowledge. As the standard
294 time constant of the RL elements is R/L , the effective time
295 constants of the model-determining transient behaviors are τ_m ,
296 τ_d , $L_a^k/R_a = f\tau_k$. Note that $L_a^k/R_a = \tau_k$ occurs only when $f \approx 1$.
297 The circuit elements and time constants are shown in Figure
298 S15.

299 To facilitate a physical interpretation of model 1 we consider
300 simplified cases. We can define conditions in which the
301 reaction time $\tau_k \approx 0$ so that f takes the equilibrium value of eq
302 4 at any moment. Then eq 2 can be simplified to eq 6 and the
303 dynamic system becomes two-dimensional, with the variables
304 u , i_c formed by eqs 1 and 6. This can be termed *diffusion-*
305 *limited transition*, model 2 in Table 3, by analogy to classical
306 electrochemistry terminology.⁵⁸ Another limiting situation is
307 when $\tau_d \approx 0$ so that eq 1 can be written as eq 7. Then the
308 dynamic system is two-dimensional also, formed by eqs 7 and
309 5 with the variables u and f . This is a *formation-limited transition*
310 mechanism, model 3.

311 By suppressing either τ_d or τ_k in the general impedance of eq
312 10, the impedance in eq 10 reduces to eq 17 that contains an
313 inductor–resistor branch, as shown in the EC of Figure 3a.
314 This circuit has been well-described before in relation to
315 inverted hysteresis in perovskite solar cells.^{9,15,59} The shape of
316 the spectra are shown in Figures 3b and S16. In the CV
317 behavior we obtain that all models 1, 2, and 3 show inductive
318 or “inverted” hysteresis^{10–14} (see Figures 2b,c and S14c–f).
319 The diffusion-limited model 2 produces a separation of
320 forward and voltage curves right at the onset of the transition,
321 leading to a shift of the effective onset voltage (Figure S14e).
322 On the other hand, for the formation-limited model 3 in Figure
323 3d the hysteresis effect occurs only when the current takes a
324 large value (Figure S14f).

325 While the large inverted hysteresis is the ordinary behavior
326 of CV of memristors, there are also cases of perovskite
327 memristors with regular hysteresis corresponding to capacitive
328 response.^{60,61} To account for such behavior we introduce in eq
329 1 the capacitive current of the interfacial transition mechanism,
330 $qN df/dt$, where N is the total number of surface sites for ions,
331 and the total possible surface charge is $Q_m = Nq$. The resulting
332 equation is indicated in eq 8, and the impedance response is
333 given by eq 18. The EC is presented in Figure 3c. The C_2 in eq

20 is the surface capacitance associated with the activation of 334
interface sites, in addition to the background capacitance C_m , 335
and R_2 in eq 19 is the associated series resistance. The time 336
constant is $\tau_2 = R_2 C_2 = L_a^k/R_a$. When $f = 1$, it is $\tau_2 = \tau_k$ by eq 13. 337
This type of serial process at intermediate frequencies has been 338
previously observed unambiguously by Ravishankar et al. in 339
IMPS measurements of MAPbBr₃ solar cells,⁶² and it was 340
interpreted as an ion accumulation process. The impedance 341
spectra show a regime of two capacitive arcs, Figure 3d, and 342
the inductive element becomes active at large voltage. 343
Consequently, the hysteresis under voltage sweep changes 344
from normal to inverted as shown in Figure 2d. Here we obtain 345
this feature experimentally by introduction of a Spiro- 346
MeOTAD layer as shown in Figure 2e. The crossing of the 347
line in the CV is also observed in the slow scan of Figure 1, 348
indicating the significance of the capacitive contribution at low 349
voltage. Finally, when the Q_m is large the CV becomes fully 350
regular (capacitive) as seen in Figure S14h. A related two- 351
capacitor circuit is shown in Figure S110 with the spectra in 352
Figure S111. 353

The dominance of RC elements at low voltage and the 354
inductive response at higher voltage can be explained by the 355
increase of the inductive time constant $f\tau_k$ after the transition 356
region, when f increases. However, the simplified models do 357
not accurately describe the impedance spectra at high voltage. 358
We therefore analyze the impedance of model 1 without 359
simplifications. The novelty in this model with respect to the 360
standard circuit of Figure 3a is the product of two R – L 361
impedances in Z_c (eq 11). The full EC is shown in Figure 3e. 362
The simulations of the impedance spectra are shown in Figures 363
3f and S17. These and other spectra for different combinations 364
of parameters can be visualized with a Mathematica program 365
presented in the Supporting Information. In the low-voltage 366
region of Figure S17b the impedance is a single RC arc. As we 367
approach the transition region of the I – u curve, in Figure S15c 368
the impedance develops the inductive loop already described 369
in Figure 3b. But Figure 3f shows a new type of spectrum not 370
found in the previous models. The behavior caused by the 371
impedance Z_c in the inductive branch increases the real part of 372
the impedance before entering the fourth quadrant. This 373
property corresponds to the high-voltage experimental spectra 374
in Figure 1. 375

If we turn to the experimental results of Figures 1 and S12, 376
we note that they show a capacitive response with one of two 377
arcs at low voltage and the generation of an inductive 378
component close to the onset of the current rise. Therefore, we 379
combine all the previous models into model 5 (Table 3) that 380
contains two inductive and two capacitive processes, as shown 381
in Figure S18, as the minimal model needed for the measured 382
memristors (see the predicted spectral shapes in Figure S19). A 383
full analysis of the spectral data shows that the impedance 384
model fits well the experimental spectra (Figure S112) and 385
provides the required parameters (Figures S113 and S114). The 386
fitting method is described in the Supporting Information, and 387
it includes the use of constant phase element exponents to 388
account for nonperfect semicircles.⁶³ An important property of 389
the model is the description of a saturation current in 390
agreement with the experimental results. By the shape of CVs, 391
it is expected that the resistance R_a decreases to a minimum 392
value when $f \approx 1/2$ as indicated in Figure S15. This is 393
confirmed by the impedance parameters, because the measured 394
 R_a decreases exponentially with a diode factor $m = 3.6$ and then 395
undergoes a saturation at large voltage (Figure S113). The 396

397 effective time constants resulting from the impedance spectra
398 fittings are shown in Figure S115. In the current transition
399 region they are reasonably constant, as assumed in the model.
400 We observe that the longest time is for the kinetic formation of
401 the high conduction effect; hence, the system is predominantly
402 formation-limited, while the ion supply is rather fast in
403 comparison.

404 The models presented in this work are designed to account
405 for the combination of internal processes in MHP memristors.
406 Our MAPbI₃ memristors are admittedly slow, with character-
407 istic times of 10 ms–1 s. The model, however, can be applied
408 to much faster time scales with adequate experimental tools
409 and the specific functions for diffusion and formation
410 characteristics that each case may require. Recently, perovskite
411 memristors for high switching speed with times of 20 ns have
412 been reported by Park et al.⁶⁴ From the measurement at
413 different duration pulses, we observe that the resistance for
414 Park et al. is larger for the larger duration pulse, in agreement
415 with our model. Therefore, we believe that the model has a
416 general significance for the analysis of the behavior of
417 memristors, even though we do not claim a universal model
418 because there is a wide variety of materials and systems, and a
419 larger investigation is needed.

420 In conclusion, we presented the results of kinetic measure-
421 ments of MAPbI₃-based memristors, and we developed a
422 three-dimensional dynamic model that describes well the
423 observed properties of voltage cycling and impedance
424 spectroscopy. The different couplings of ionic and electronic
425 phenomena are characterized by capacitive and inductive
426 features that generate new impedance functions in agreement
427 with the experimental measurements. We also describe well the
428 changes from regular to inverted hysteresis by the dominance
429 of capacitive or inductive elements, respectively. It is not
430 possible to know the formation of diffusion mechanisms a
431 priori, but the essential progress we provide here is the need to
432 separate them, finding the consequences of their compositions
433 on experimental measurements.

434 ■ ASSOCIATED CONTENT

435 **SI** Supporting Information

436 The Supporting Information is available free of charge at
437 <https://pubs.acs.org/doi/10.1021/acseenergylett.2c00121>.

438 Materials and device preparation; details of models;
439 impedance spectra fitting resources and results;
440 Mathematica program to represent current–voltage
441 curves and impedance spectra (PDF)

442 ■ AUTHOR INFORMATION

443 Corresponding Author

444 **Juan Bisquert** – Institute of Advanced Materials (INAM),
445 Universitat Jaume I, 12006 Castelló, Spain; *Yonsei Frontier*
446 *Lab, Yonsei University, Seoul 03722, South Korea*;
447 orcid.org/0000-0003-4987-4887; Email: bisquert@uji.es

448 Authors

449 **Mariana Berruet** – Institute of Advanced Materials (INAM),
450 Universitat Jaume I, 12006 Castelló, Spain; *División*
451 *Electroquímica Aplicada, INTEMA, CONICET, Universidad*
452 *Nacional de Mar del Plata, B7606BWV Mar del Plata,*
453 *Argentina*
454 **José Carlos Pérez-Martínez** – Institute of Advanced Materials
455 (INAM), Universitat Jaume I, 12006 Castelló, Spain;

Electronic Technology Area, Universidad Rey Juan Carlos, 456
28933 Móstoles, Spain 457

Beatriz Romero – *Electronic Technology Area, Universidad* 458
Rey Juan Carlos, 28933 Móstoles, Spain 459

Cedric Gonzales – *Institute of Advanced Materials (INAM),* 460
Universitat Jaume I, 12006 Castelló, Spain; orcid.org/0000-0002-6550-2007 461
462

Abdullah Al-Mayouf – *Chemistry Department, College of* 463
Science, King Saud University, Riyadh 11451, Saudi Arabia; 464
orcid.org/0000-0001-9246-7684 465

Antonio Guerrero – *Institute of Advanced Materials* 466
(INAM), Universitat Jaume I, 12006 Castelló, Spain; 467
orcid.org/0000-0001-8602-1248 468

Complete contact information is available at: 469
<https://pubs.acs.org/doi/10.1021/acseenergylett.2c00121> 470

471 Notes

The authors declare no competing financial interest. 472

473 ■ ACKNOWLEDGMENTS

We acknowledge the financial support from Generalitat 474
Valenciana for a Grisolia grant (GRISOLIAP/2019/048) and 475
Ministerio de Ciencia y Innovación (PID2019-107348GB- 476
100). We also acknowledge the financial support of CONICET 477
(Extern Fellowship 2020); Comunidad de Madrid (S2018/ 478
NMT-4326-SINFOTON2-CM); and Universidad Rey Juan 479
Carlos “Grupo DELFO de alto rendimiento”, reference 480
M2363, under research program “Programa de fomento y 481
desarrollo de la investigación”. 482

483 ■ REFERENCES

- (1) Kojima, A.; Teshima, K.; Shirai, Y.; Miyasaka, T. Organometal 484
halide perovskites as visible-light sensitizers for photovoltaic cells. *J.* 485
Am. Chem. Soc. **2009**, *131*, 6050–6051. 486
- (2) *Organic-Inorganic Halide Perovskite Photovoltaics: From Funda-* 487
mentals to Device Architectures; Park, N.-G., Grätzel, M., Miyasaka, T., 488
Eds.; Springer, 2016. 489
- (3) Nayak, P. K.; Mahesh, S.; Snaith, H. J.; Cahen, D. Photovoltaic 490
solar cell technologies: analysing the state of the art. *Nat. rev. Mater.* 491
2019, *4*, 269–285. 492
- (4) Kim, J. Y.; Lee, J.-W.; Jung, H. S.; Shin, H.; Park, N.-G. High- 493
Efficiency Perovskite Solar Cells. *Chem. Rev.* **2020**, *120*, 7867–7918. 494
- (5) Azpiroz, J. M.; Mosconi, E.; Bisquert, J.; De Angelis, F. Defect 495
migration in methylammonium lead iodide and its role in perovskite 496
solar cell operation. *Energy Environ. Sci.* **2015**, *8*, 2118–2127. 497
- (6) Senocrate, A.; Maier, J. Solid-State Ionics of Hybrid Halide 498
Perovskites. *J. Am. Chem. Soc.* **2019**, *141*, 8382–8396. 499
- (7) Lopez-Varo, P.; Jiménez-Tejada, J. A.; García-Rosell, M.; 500
Ravishankar, S.; Garcia-Belmonte, G.; Bisquert, J.; Almora, O. Device 501
Physics of Hybrid Perovskite Solar cells: Theory and Experiment. *Adv.* 502
Energy Mater. **2018**, *8*, 1702772. 503
- (8) Zhang, T.; Hu, C.; Yang, S. Ion Migration: A “Double-Edged 504
Sword” for Halide-Perovskite-Based Electronic Devices. *Small* 505
Methods **2020**, *4*, 1900552. 506
- (9) Bisquert, J.; Guerrero, A.; Gonzales, C. Theory of Hysteresis in 507
Halide Perovskites by Integration of the Equivalent Circuit. *ACS Phys.* 508
Chem. Au **2021**, *1*, 25–44. 509
- (10) Almora, O.; Aranda, C.; Zarazua, I.; Guerrero, A.; Garcia- 510
Belmonte, G. Noncapacitive Hysteresis in Perovskite Solar Cells at 511
Room Temperature. *ACS Energy Lett.* **2016**, *1*, 209–215. 512
- (11) Rong, Y. G.; Hu, Y.; Ravishankar, S.; Liu, H. W.; Hou, X. M.; 513
Sheng, Y. S.; Mei, A. Y.; Wang, Q. F.; Li, D. Y.; Xu, M.; Bisquert, J.; 514
Han, H. W. Tunable hysteresis effect for perovskite solar cells. *Energy* 515
Environ. Sci. **2017**, *10*, 2383–2391. 516

- (12) Tress, W.; Correa Baena, J. P.; Saliba, M.; Abate, A.; Graetzel, M. Inverted Current–Voltage Hysteresis in Mixed Perovskite Solar Cells: Polarization, Energy Barriers, and Defect Recombination. *Adv. Energy Mater.* **2016**, *6*, 1600396.
- (13) Wu, F.; Pathak, R.; Chen, K.; Wang, G.; Bahrami, B.; Zhang, W.-H.; Qiao, Q. Inverted Current–Voltage Hysteresis in Perovskite Solar Cells. *ACS Energy Lett.* **2018**, *3*, 2457–2460.
- (14) Alvarez, A. O.; Arcas, R.; Aranda, C. A.; Bethencourt, L.; Mas-Marzá, E.; Saliba, M.; Fabregat-Santiago, F. Negative Capacitance and Inverted Hysteresis: Matching Features in Perovskite Solar Cells. *J. Phys. Chem. Lett.* **2020**, *11*, 8417–8423.
- (15) Guerrero, A.; Bisquert, J.; Garcia-Belmonte, G. Impedance spectroscopy of metal halide perovskite solar cells from the perspective of equivalent circuits. *Chem. Rev.* **2021**, *121*, 14430–14484.
- (16) Kwak, K. J.; Lee, D. E.; Kim, S. J.; Jang, H. W. Halide Perovskites for Memristive Data Storage and Artificial Synapses. *J. Phys. Chem. Lett.* **2021**, *12*, 8999–9010.
- (17) Kang, K.; Hu, W.; Tang, X. Halide Perovskites for Resistive Switching Memory. *J. Phys. Chem. Lett.* **2021**, *12*, 11673–11682.
- (18) Fang, Y.; Zhai, S.; Chu, L.; Zhong, J. Advances in Halide Perovskite Memristor from Lead-Based to Lead-Free Materials. *ACS Appl. Mater. Int.* **2021**, *13*, 17141–17157.
- (19) Pershin, Y. V.; Di Ventra, M. Memory effects in complex materials and nanoscale systems. *Adv. Phys.* **2011**, *60*, 145–227.
- (20) Rahimi Azghadi, M.; Chen, Y.-C.; Eshraghian, J. K.; Chen, J.; Lin, C.-Y.; Amirsoleimani, A.; Mehonic, A.; Kenyon, A. J.; Fowler, B.; Lee, J. C.; Chang, Y.-F. Complementary Metal-Oxide Semiconductor and Memristive Hardware for Neuromorphic Computing. *Advanced Intelligent Systems* **2020**, *2*, 1900189.
- (21) Gogoi, H. J.; Bajpai, K.; Mallajosyula, A. T.; Solanki, A. Advances in Flexible Memristors with Hybrid Perovskites. *J. Phys. Chem. Lett.* **2021**, *12*, 8798–8825.
- (22) Zhao, X.; Xu, H.; Wang, Z.; Lin, Y.; Liu, Y. Memristors with organic-inorganic halide perovskites. *InfoMat* **2019**, *1*, 183–210.
- (23) Poddar, S.; Zhang, Y.; Gu, L.; Zhang, D.; Zhang, Q.; Yan, S.; Kam, M.; Zhang, S.; Song, Z.; Hu, W.; Liao, L.; Fan, Z. Down-Scalable and Ultra-fast Memristors with Ultra-high Density Three-Dimensional Arrays of Perovskite Quantum Wires. *Nano Lett.* **2021**, *21*, 5036–5044.
- (24) Kim, H.; Han, J. S.; Kim, S. G.; Kim, S. Y.; Jang, H. W. Halide perovskites for resistive random-access memories. *J. Mater. Chem. C* **2019**, *7*, 5226–5234.
- (25) Zamarreño-Ramos, C.; Serrano-Gotarredona, T.; Camuñas-Mesa, L.; Perez-Carrasco, J.; Masquelier, T.; Linares-Barranco, B. On Spike-Timing-Dependent-Plasticity, Memristive Devices, and Building a Self-Learning Visual Cortex. *Frontiers Neurosci.* **2011**, *5*, 26.
- (26) Covi, E.; Brivio, S.; Serb, A.; Prodromakis, T.; Fanciulli, M.; Spiga, S. Analog Memristive Synapse in Spiking Networks Implementing Unsupervised Learning. *Front. Neurosci.* **2016**, *10*, 482.
- (27) John, R. A.; Yantara, N.; Ng, S. E.; Patdillah, M. I. B.; Kulkarni, M. R.; Jamaludin, N. F.; Basu, J.; Ankit; Mhaisalkar, S. G.; Basu, A.; Mathews, N. Diffusive and Drift Halide Perovskite Memristive Barristors as Nociceptive and Synaptic Emulators for Neuromorphic Computing. *Adv. Mater.* **2021**, *33*, 2007851.
- (28) Xu, W.; Cho, H.; Kim, Y.-H.; Kim, Y.-T.; Wolf, C.; Park, C.-G.; Lee, T.-W. Organometal Halide Perovskite Artificial Synapses. *Adv. Mater.* **2016**, *28*, 5916–5922.
- (29) Xiao, Z.; Huang, J. Energy-Efficient Hybrid Perovskite Memristors and Synaptic Devices. *Adv. Electron. Mater.* **2016**, *2*, 1600100.
- (30) Christensen, D. V.; Dittmann, R.; Linares-Barranco, B.; Sebastian, A.; Le Gallo, M. 2022 roadmap on neuromorphic computing and engineering. *Neuromorphic Computing and Engineering* **2022**. DOI: 10.1088/2634-4386/ac4a83
- (31) Choi, J.; Han, J. S.; Hong, K.; Kim, S. Y.; Jang, H. W. Organic–Inorganic Hybrid Halide Perovskites for Memories, Transistors, and Artificial Synapses. *Adv. Mater.* **2018**, *30*, 1704002.
- (32) Yang, J.-Q.; Wang, R.; Wang, Z.-P.; Ma, Q.-Y.; Mao, J.-Y.; Ren, 585 Y.; Yang, X.; Zhou, Y.; Han, S.-T. Leaky integrate-and-fire neurons 586 based on perovskite memristor for spiking neural networks. *Nano 587 Energy* **2020**, *74*, 104828. 588
- (33) Yang, X.; Xiong, Z.; Chen, Y.; Ren, Y.; Zhou, L.; Li, H.; Zhou, 589 Y.; Pan, F.; Han, S.-T. A self-powered artificial retina perception 590 system for image preprocessing based on photovoltaic devices and 591 memristive arrays. *Nano Energy* **2020**, *78*, 105246. 592
- (34) Kim, M. S.; Kim, M. S.; Lee, G. J.; Sunwoo, S.-H.; Chang, S.; 593 Song, Y. M.; Kim, D.-H. Bio-Inspired Artificial Vision and 594 Neuromorphic Image Processing Devices. *Advanced Materials 595 Technologies* **2022**, *7*, 2100144. 596
- (35) Gong, J.; Wei, H.; Ni, Y.; Zhang, S.; Du, Y.; Xu, W. 597 Methylammonium halide-doped perovskite artificial synapse for light- 598 assisted environmental perception and learning. *Materials Today 599 Physics* **2021**, *21*, 100540. 600
- (36) von Hauff, E. Impedance Spectroscopy for Emerging 601 Photovoltaics. *J. Phys. Chem. C* **2019**, *123*, 11329–11346. 602
- (37) Bisquert, J.; Janssen, M. From Frequency Domain to Time 603 Transient Methods for Halide Perovskite Solar Cells: The 604 Connections of IMPS, IMVS, TPC and TPV. *J. Phys. Chem. Lett. 605 2021*, *12*, 7964–7971. 606
- (38) Solanki, A.; Guerrero, A.; Zhang, Q.; Bisquert, J.; Sum, T. C. 607 Interfacial Mechanism for Efficient Resistive Switching in Rud- 608 dlesden-Popper Perovskites for Non-Volatile Memories. *J. Phys. Chem. 609 Lett.* **2020**, *11*, 463–470. 610
- (39) Gonzales, C.; Guerrero, A.; Bisquert, J. Spectral properties of 611 the dynamic state transition in metal halide perovskite-based 612 memristor exhibiting negative capacitance. *Appl. Phys. Lett.* **2021**, 613 *118*, 073501. 614
- (40) Lanza, M.; Wong, H. S. P.; Pop, E.; Ielmini, D.; Strukov, D.; 615 Regan, B. C.; Larcher, L.; Villena, M. A.; Yang, J. J.; Goux, L.; 616 Belmonte, A.; Yang, Y.; Puglisi, F. M.; Kang, J.; Magyari-Köpe, B.; 617 Yalon, E.; Kenyon, A.; Buckwell, M.; Mehonic, A.; Shluger, A.; Li, H.; 618 Hou, T.-H.; Hudec, B.; Akinwande, D.; Ge, R.; Ambrogio, S.; Roldan, 619 J. B.; Miranda, E.; Suñe, J.; Pey, K. L.; Wu, X.; Raghavan, N.; Wu, E.; 620 Lu, W. D.; Navarro, G.; Zhang, W.; Wu, H.; Li, R.; Holleitner, A.; 621 Wurstbauer, U.; Lemme, M. C.; Liu, M.; Long, S.; Liu, Q.; Lv, H.; 622 Padovani, A.; Pavan, P.; Valov, I.; Jing, X.; Han, T.; Zhu, K.; Chen, S.; 623 Hui, F.; Shi, Y. Recommended Methods to Study Resistive Switching 624 Devices. *Adv. Electron. Mater.* **2019**, *5*, 1800143. 625
- (41) Zohar, A.; Kedem, N.; Levine, I.; Zohar, D.; Vilan, A.; Ehre, D.; 626 Hodes, G.; Cahen, D. Impedance Spectroscopic Indication for Solid 627 State Electrochemical Reaction in (CH₃NH₃)PbI₃ Films. *J. Phys. 628 Chem. Lett.* **2016**, *7*, 191–197. 629
- (42) Khan, M. T.; Huang, P.; Almomhammedi, A.; Kazim, S.; Ahmad, 630 S. Mechanistic origin and unlocking of negative capacitance in 631 perovskites solar cells. *iScience* **2021**, *24*, 102024. 632
- (43) Fabregat-Santiago, F.; Kulbak, M.; Zohar, A.; Vallés-Pelarda, 633 M.; Hodes, G.; Cahen, D.; Mora-Seró, I. Deleterious Effect of 634 Negative Capacitance on the Performance of Halide Perovskite Solar 635 Cells. *ACS Energy Lett.* **2017**, *2*, 2007–2013. 636
- (44) Izhikevich, E. M. *Dynamical Systems in Neuroscience*; MIT Press, 637 2007. 638
- (45) Bisquert, J. A frequency domain analysis of excitability and 639 bifurcations of Fitzhugh-Nagumo neuron model. *J. Phys. Chem. Lett. 640 2021*, *12*, 11005–11013. 641
- (46) Kuehn, C. *Multiple Time Scale Dynamics*; Springer, 2015. 642
- (47) Nagumo, J.; Arimoto, S.; Yoshizawa, S. An Active Pulse 643 Transmission Line Simulating Nerve Axon. *Proceedings of the IRE 644 1962*, *50*, 2061–2070. 645
- (48) Hodgkin, A. L.; Huxley, A. F. A quantitative description of 646 membrane current and its application to conduction and excitation in 647 nerve. *J. Physiol* **1952**, *117*, 500–544. 648
- (49) Wallisch, P.; Lusignan, M. E.; Benayoun, M. D.; Baker, T. I.; 649 Dickey, A. S.; Hatsopoulos, N. H. *MATLAB for Neurosciences*; 650 Elsevier, 2014. 651
- (50) Yang, J. J.; Strukov, D. B.; Stewart, D. R. Memristive devices for 652 computing. *Nat. Nanotechnol.* **2013**, *8*, 13–24. 653

- 654 (51) Bou, A.; Bisquert, J. Impedance spectroscopy dynamics of
655 biological neural elements: from memristors to neurons and synapses.
656 *J. Phys. Chem. B* **2021**, *125*, 9934–9949.
- 657 (52) Chua, L. Memristor, Hodgkin–Huxley, and Edge of Chaos.
658 *Nanotechnology* **2013**, *24*, 383001.
- 659 (53) Bisquert, J. *The Physics of Solar Energy Conversion*; CRC Press:
660 Boca Raton, FL, 2020.
- 661 (54) Kang, D.-H.; Park, N.-G. On the Current–Voltage Hysteresis
662 in Perovskite Solar Cells: Dependence on Perovskite Composition
663 and Methods to Remove Hysteresis. *Adv. Mater.* **2019**, *31*, 1805214.
- 664 (55) Unger, E. L.; Hoke, E. T.; Bailie, C. D.; Nguyen, W. H.;
665 Bowring, A. R.; Heumuller, T.; Christoforo, M. G.; McGehee, M. D.
666 Hysteresis and transient behavior in current-voltage measurements of
667 hybrid-perovskite absorber solar cells. *Energy Environ. Sci.* **2014**, *7*,
668 3690–3698.
- 669 (56) Snaith, H. J.; Abate, A.; Ball, J. M.; Eperon, G. E.; Leijtens, T.;
670 Noel, N. K.; Stranks, S. D.; Wang, J. T.-W.; Wojciechowski, K.;
671 Zhang, W. Anomalous Hysteresis in Perovskite Solar Cells. *J. Phys.*
672 *Chem. Lett.* **2014**, *5*, 1511–1515.
- 673 (57) Kim, H.-S.; Jang, I.-H.; Ahn, N.; Choi, M.; Guerrero, A.;
674 Bisquert, J.; Park, N.-G. Control of I-V Hysteresis in CH₃NH₃PbI₃
675 Perovskite Solar Cell. *J. Phys. Chem. Lett.* **2015**, *6*, 4633–4639.
- 676 (58) Bard, A. J.; Faulkner, L. R. *Electrochemical Methods*,
677 *Fundamentals and Applications*, 2nd ed.; John Wiley & Sons:
678 Weinheim, Germany, 2001.
- 679 (59) Ghahremanirad, E.; Bou, A.; Olyae, S.; Bisquert, J. Inductive
680 Loop in the Impedance Response of Perovskite Solar Cells Explained
681 by Surface Polarization Model. *J. Phys. Chem. Lett.* **2017**, *8*, 1402–
682 1406.
- 683 (60) Wang, S.; Xiong, Y.; Dong, X.; Sha, J.; Wu, Y.; Li, W.; Wang, Y.
684 Capacitive coupling behaviors based on triple cation organic-inorganic
685 hybrid perovskite memristor. *J. Alloys Compd.* **2021**, *874*, 159884.
- 686 (61) Chua, L. Resistance switching memories are memristors. *Appl.*
687 *Phys. A: Mater. Sci. Process.* **2011**, *102*, 765–783.
- 688 (62) Ravishankar, S.; Aranda, C.; Sanchez, S.; Bisquert, J.; Saliba, M.;
689 Garcia-Belmonte, G. Perovskite Solar Cell Modeling Using Light and
690 Voltage Modulated Techniques. *J. Phys. Chem. C* **2019**, *123*, 6444–
691 6449.
- 692 (63) Lasia, A. The Origin of the Constant Phase Element. *J. Phys.*
693 *Chem. Lett.* **2022**, *13*, 580–589.
- 694 (64) Park, Y.; Kim, S. H.; Lee, D.; Lee, J.-S. Designing zero-
695 dimensional dimer-type all-inorganic perovskites for ultra-fast switch-
696 ing memory. *Nat. Commun.* **2021**, *12*, 3527.